



HAL
open science

Solid Circulation Study in a 1.5 MWth Cold Flow Model of Chemical Looping Combustion

Hu Chen, Zhenshan Li, Xinglei Liu, Weicheng Li, Ningsheng Cai, Stéphane Bertholin, Sina Tebianian, Mahdi Yazdanpanah, Aoling Zhang

► **To cite this version:**

Hu Chen, Zhenshan Li, Xinglei Liu, Weicheng Li, Ningsheng Cai, et al.. Solid Circulation Study in a 1.5 MWth Cold Flow Model of Chemical Looping Combustion. *Industrial and engineering chemistry research*, 2021, 60 (5), pp.2265-2277. 10.1021/acs.iecr.0c04611 . hal-03250102

HAL Id: hal-03250102

<https://ifp.hal.science/hal-03250102>

Submitted on 4 Jun 2021

HAL is a multi-disciplinary open access archive for the deposit and dissemination of scientific research documents, whether they are published or not. The documents may come from teaching and research institutions in France or abroad, or from public or private research centers.

L'archive ouverte pluridisciplinaire **HAL**, est destinée au dépôt et à la diffusion de documents scientifiques de niveau recherche, publiés ou non, émanant des établissements d'enseignement et de recherche français ou étrangers, des laboratoires publics ou privés.

Solid circulation study in a 1.5 MW_{th} cold flow model of chemical looping combustion

Hu Chen¹, Zhenshan Li^{1*}, Xinglei Liu², Weicheng Li², Ningsheng Cai¹, Stéphane Bertholin³, Sina Tebianian³, Mahdi Yazdanpanah⁴, Aoling Zhang⁴

¹Key Laboratory for Thermal Science and Power Engineering of Ministry of Education, Department of Energy and Power Engineering, Tsinghua University, Beijing 100084, China

²Clean Combustion and Flue Gas Purification Key Laboratory of Sichuan Province, Dongfang Boiler Co., Ltd., Dongfang Electric Group, Zigong 643099, Sichuan, China

³IFP Énergies Nouvelles, Rond-point échangeur de Solaize, 69360 Solaize, France

⁴TOTAL, Research & Technology Gonfreville (TRTG), 76700 Harfleur, France

Corresponding author: E-mail: lizs@mail.tsinghua.edu.cn; Tel.: +86 010-62792478.

Abstract

Solid circulation in chemical looping combustion (CLC) is very important and affects the mass and heat balance and auto-thermal operation of a CLC system. A key task in developing CLC technology is to control the solid circulation. In this work, the solid circulation characteristic of a 1.5 MW_{th} CLC cold flow model is reported. The solid circulation between the fuel reactor and the simplified air reactor riser is controlled by the overflow method. Three kinds of quartz sands are selected as fluidized particles, and their median particle diameters are 392 μm, 249 μm and 122 μm, respectively. Reasonable pressure profile is obtained in the 1.5 MW_{th} CLC cold flow model. The effects of operational parameters, including the fuel reactor gas velocity, loop seal gas velocity, simplified riser gas velocity, particle size and static bed height, on the solid circulation and hydrodynamic characteristics are measured and analyzed. The maximum solid circulation rate can approach 130 kg/(m²·s), and this value satisfies the

* Corresponding author. Tel.: +86 010-62792478
E-mail address: lizs@mail.tsinghua.edu.cn

requirements of mass and heat balance in CLC system. The static bed height in the fuel reactor should be higher than the overflow port to prevent it from becoming a constraint factor on the solid circulation rate. An overflow model is developed to predict the solid circulation rate, and the relative errors between the predicted result and the experimental data are within 25%.

Highlights:

1. A 1.5 MW_{th} CLC cold flow model is designed and constructed;
2. The maximum solid circulation rate can approach 130 kg/(m²·s), and this value satisfies the requirements of CLC auto-thermal operation;
3. The static bed height should be higher than the overflow port to obtain a high solid circulation rate;
4. An overflow model is developed to predict the solid circulation rate, and the relative errors are within 25%.

1. Introduction

CO₂ is considered to be a main greenhouse gas causing climate change and global warming ¹. The International Energy Agency has estimated that energy-related CO₂ emissions have risen 1.4% and have reached a historic high of 32.5 Gt ². This worldwide concern has continuously aroused extensive research towards developing more efficient and economical technology for CO₂ capture in term of environmentally sound approaches ^{3,4}. Recently, chemical looping combustion (CLC) has been regarded as a promising technology because it enables CO₂ capture in a fossil fuel combustion process with nearly no energy penalties ⁵. A CLC unit is primarily composed of a fuel reactor (FR) and an air reactor (AR), and an appropriate solid metal oxide as an oxygen carrier (OC) is circulated between the two reactors to transfer lattice oxygen to fossil fuel.

Richter and Knoche ⁶ first proposed the concept of CLC in 1983, and since then it has been widely applied to the combustion field ⁷⁻⁹. For a CLC unit, choosing an appropriate reactor type is important because it is related to the chemical reaction and operation of the CLC unit. Presently, based on gas-solid hydrodynamic characteristics, CLC units have three reactor types, namely, fluidized bed as air reactor-moving bed as fuel reactor, moving bed as air reactor-fluidized bed as fuel reactor, and fluidized bed as air reactor-fluidized bed as fuel reactor which is also known as two interconnected fluidized beds ¹⁰. For the fluidized bed as air reactor-moving bed as fuel reactor, only Ohio State University has adopted this approach in a 25 kW_{th} CLC unit ¹¹. For the moving bed as air reactor-fluidized bed as fuel reactor, only Southeast University has adopted this approach in a 20 kW_{th} CLC unit ¹². The two interconnected fluidized beds approach has been employed by many research institutes as a CLC pilot plant reactor

type, such as the 10 kW_{th}⁸ and 100 kW_{th}¹³ units at Chalmers University of Technology, the 50 kW_{th} unit at Instituto de Carboquímica¹⁴, the 10 kW_{th} unit at Southeast University¹⁵, the 10 kW_{th} unit at IFP Énergies Nouvelles¹⁶, the 50 kW_{th} unit at Huazhong University of Science and Technology¹⁷, the 10 kW_{th} unit at Tsinghua University¹⁸, the 225 kW_{th} unit at University of Utah¹⁹, the 1 MW_{th} unit at Darmstadt University of Technology²⁰, and the 3 MW_{th} unit at Alstom Power²¹. Therefore, the two interconnected fluidized beds are the dominant reactor type used for CLC technology.

In the two interconnected fluidized beds, the gas-solid hydrodynamic characteristics, especially solid circulation control, are significant to the operation of the CLC pilot plant. The temperature difference between the AR and FR, chemical reactions and heat and mass balance are affected by the solid circulation characteristics. Solid circulation must be right for the two interconnected fluidized beds. If the solid circulation rate is too low, the heat balance cannot be satisfied, resulting in a loss in fuel reactor temperature; if the solid circulation rate is too high, the residence time in the fuel reactor will be decreased, resulting in a loss in CO₂ capture. There are three types of solid circulation principles for the two interconnected fluidized beds: double loop control, hydraulic connection and overflow exit from the fuel reactor²²⁻²⁴. Some cold flow models have been built to investigate the hydrodynamic characteristics and solid circulation of the two interconnected fluidized beds. Stollhof et al.²⁵ adopted the hydraulic connection principle to study the effect of four different FR designs on CLC hydrodynamics, and they found that the shape of the conical form of the FR bottom part would affect FR hydrodynamics and led to unstable hydrodynamics in some cases, while AR hydrodynamics was not affected by changes in FR design. Dubey et al.²⁶ constructed a cold flow model based on the overflow exit from the fuel reactor principle

and used Indian ilmenite as an oxygen carrier to investigate the effect of riser gas velocity on the voidage profiles, solid circulation rate, and pressure profiles. Bischi et al.²⁷ selected the double loop control and hydraulic connection principle in a 150 kW_{th} cold flow model to study the change trend of CLC hydrodynamics under different loads, gas velocities and solid return styles. To study the feasibility of a proposed dual fluidized bed, Liu et al.²⁸ constructed a cold flow model based on the hydraulic connection principle to study the effect of the total solid inventory and fluidization number of loop seal (LS) on the solid recirculation flux and solid fraction. Alghamdi et al.²⁹ constructed a 10 kW_{th} CLC unit and a 200 kW_{th} CLC unit based on the overflow exit from the fuel reactor principle to demonstrate the hydrodynamic similarities. In the two interconnected fluidized beds, controlling solid circulation by using the overflow principle has been widely adopted, such as the 10 kW_{th}⁸ and 100 kW_{th}¹³ units at Chalmers University of Technology, the 25 kW_{th} unit at Hamburg University of Technology³⁰, the 10 kW_{th} unit at University of Stuttgart³¹, the 10 kW_{th} unit at Southeast University¹⁵ and the 225 kW_{th} unit at University of Utah¹⁹. Most of the reported works on CLC hydrodynamics have been conducted with different gas velocities, total solid inventories, particle sizes and solid return styles in small lab-scale setups. However, few studies have focused on the effect of the overflow port fluidization regime on CLC hydrodynamics in large-scale units.

In this work, a 1.5 MW_{th} CLC cold flow model is proposed and constructed to study the overflow hydrodynamics and solid circulation control. The effects of different gas velocities, particle sizes and static bed heights on the solid circulation rate and fluidization characteristics are studied. An overflow model is proposed to predict the solid circulation rate.

2. Experiments

2.1 Experimental setup

The schematic diagram of the 1.5 MW_{th} CLC cold flow model system is shown in Figure 1. The fuel reactor is composed of a turbulent fluidized bed (TFB), a FR riser and an annular carbon stripper (CS), and the specific dimensions of the fuel reactor have been provided in previous work³². An overflow port is located on the side of the TFB with a height of 1.25 m, an inner diameter of 0.15 m and a downward opening. A loop seal is connected with the overflow port and a simplified air reactor riser. The simplified riser (SR) has a height of 10.45 m and an inner diameter of 0.18 m. The purpose of the simplified riser is to transport solid particles from the overflow port back to the fuel reactor to achieve continuous operation of the cold flow model. The FR cyclone is shared by the FR and SR. The inner diameter of the dipleg is 0.15 m, and a butterfly valve is installed to measure the solid circulation rate by the volume method.

The solid particles from the hopper are fed into the TFB. After a certain residence time in the TFB, most of the solid particles are transported to the SR through the overflow port and loop seal, while a few of them are elutriated into the annular CS. The solid particles from both the SR (G_s) and annular CS ($G_{s,FR}$) are transported to the top of the cold flow model by fluidizing air. The mixed solid particles ($G_{s,t}$) from the annular CS and SR enter into the FR cyclone. The gas velocity at the FR top (~ 6 m/s) is higher than the terminal velocity of solid particles, which ensures that the solid particles from the SR will not enter into the annular CS but directly enter into the FR cyclone. Then, the solid particles are separated by the FR cyclone and returned back to the TFB. In the 1.5 MW_{th} CLC cold flow model, 31 pressure ports and 35 pressure transmitters are installed to measure pressure profiles. Pressure data is read and stored every 1 s for at

least 5 min in stable operation before changing to the next test. Four sampling devices are separately installed on the TFB, annular CS, SR and loop seal for collecting sample particles.

The fluidizing air of the FR and SR are supplied by a Roots blower in which the maximum pressure and flowrate are 68 kPa and 10000 Nm³/h, respectively. The fluidizing air of the TFB, annular CS and SR are controlled by pneumatic valves because their air volumes need to be changed frequently, and their flowrates are measured by vortex flowmeters. The fluidizing air of loop seals are provided by an air compressor in which the maximum pressure and flowrate are 0.8 MPa and 600 Nm³/h, and the flowrates are regulated by float flowmeters.

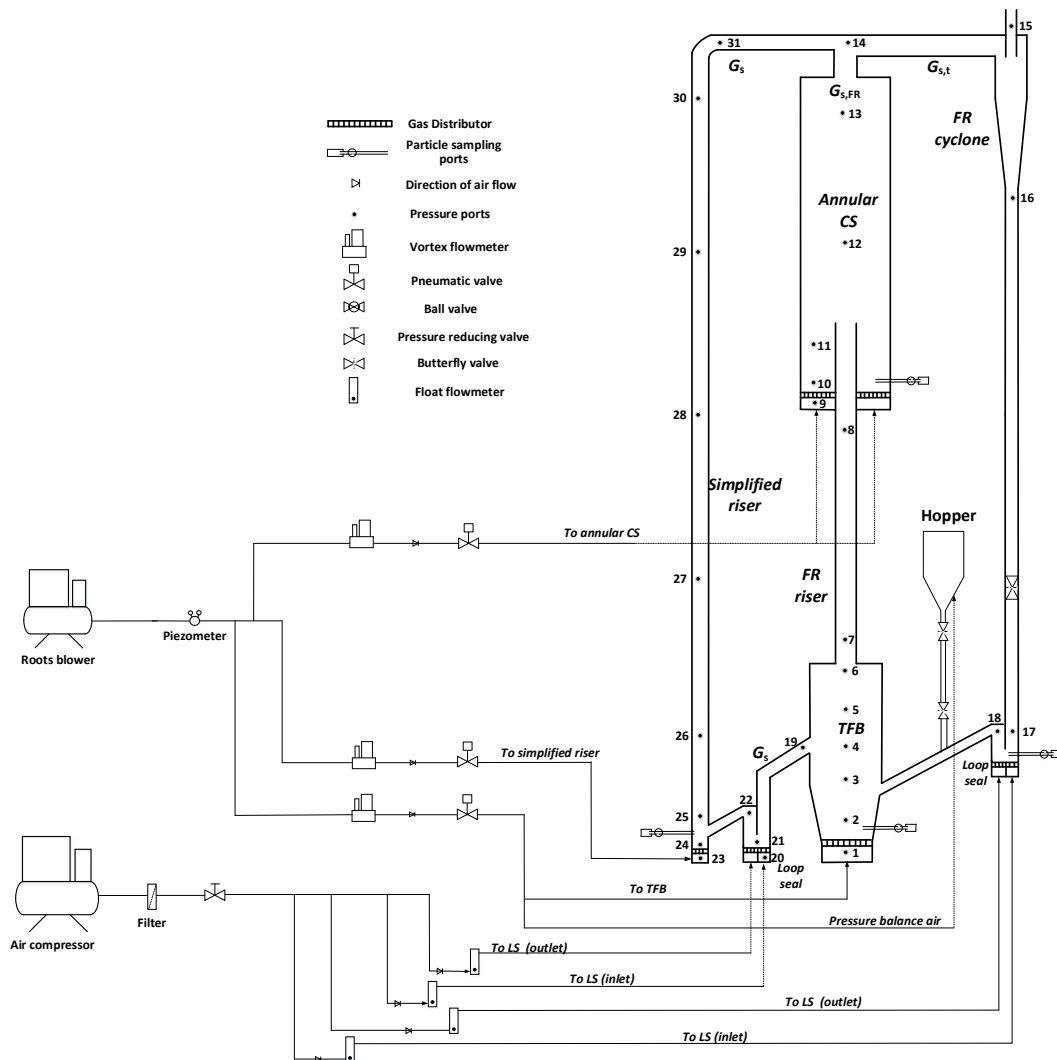


Figure 1. Schematic diagram of the 1.5 MW_{th} CLC cold flow model

2.2 Materials

Three kinds of quartz sands are chosen to investigate the overflow hydrodynamics of different particle sizes. The properties of the three quartz sands are listed in Table 1³²⁻³⁴. The particle size distributions (PSDs) are measured by using a Malvern Mastersizer, and the results are shown in Figure 2.

Table 1. The properties of three kinds of quartz sands

Item	Unit	$d_{50}=122\ \mu\text{m}$	$d_{50}=249\ \mu\text{m}$	$d_{50}=392\ \mu\text{m}$
Bulk density	kg/m^3	1396	1390	1377
Particle density	kg/m^3	2715	2716	2702
Geldart classification	-	B	B	B
Minimum fluidization velocity ³³	m/s	0.01	0.06	0.13
Terminal velocity ³⁴	m/s	0.85	2.23	3.55
Transition velocity ³²	m/s	0.78	0.95	1.06

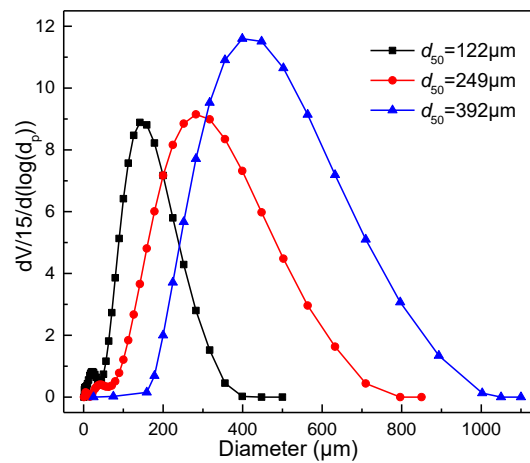


Figure 2. Particle size distributions of three kinds of quartz sands

2.3 Data evaluation

The solid fraction (ε_s) is derived by the pressure drop, and the equation is as follows:

$$\Delta P/\Delta H = \rho_p \varepsilon_s g + \rho_g (1 - \varepsilon_s) g \quad (1)$$

where $\Delta P/\Delta H$ represents the pressure gradient, Pa/m; g is the gravity acceleration, m/s²; and ρ_p and ρ_g represent the particle density and gas density, respectively, kg/m³.

Based on the mass balance, the solid circulation rate of the overflow port is equal to that of the SR. As shown in Figure 1, the solid circulation rate of the SR (hereinafter referred to as the solid circulation rate, G_s) is defined as the total solid circulation rate ($G_{s,t}$) minus the FR solid circulation rate ($G_{s,FR}$):

$$G_s = G_{s,t} - G_{s,FR} \quad (2)$$

Both the $G_{s,t}$ and $G_{s,FR}$ are measured by the accumulative volume method. When the cold flow model operates steadily, the accumulative height and elapsed time in the dipleg are measured after closing the butterfly valve, and the $G_{s,t}$ can be calculated by equation (3). Then, turn off the fluidizing gas of the loop seal between FR and SR and measure the $G_{s,FR}$ using the same method, as shown in equation (4). The results of the $G_{s,FR}$ have been provided in previous work³². It should be noted that the value of the FR solid circulation rate in the literature³² is calculated based on the sectional area of the annular CS, while the $G_{s,FR}$ in this work is calculated based on the sectional area of the simplified riser, so the literature value needs to be converted.

$$G_{s,t} = \frac{\rho_b S_{dip} H_{dip,t}}{S_{SR} t_{dip,t}} \quad (3)$$

$$G_{s,FR} = \frac{\rho_b S_{dip} H_{dip,FR}}{S_{SR} t_{dip,FR}} \quad (4)$$

where S_{dip} is the sectional area of the dipleg, m²; ρ_b is the bulk density, kg/m³; $H_{dip,i}$ is the accumulative height of solid particles in the dipleg, m; S_{SR} is the sectional

area of the simplified riser, m^2 ; and $t_{dip,i}$ is the elapsed time of solid particles in the dipleg, s.

3. Results

3.1 Stable operation results

The pressure profile of the 1.5 MW_{th} CLC cold flow model is depicted in Figure 3. The pressure drops of loop seals (P18-P4, P22-P25) were all positive, and the pressure of the FR and SR decreased with increasing the reactor height. The results indicated that a reasonable pressure balance was obtained in this cold flow model. Most of the particles accumulated in the FR dense phase because the pressure drops (P1-P5, P9-P12) were high, as shown in Figure 3. The pressure drop in the SR dense phase (P23-P25) was relatively low (4.41 kPa), and the sectional area of the SR was 0.025 m², so only a small amount of particles accumulated there. Comparing the pressure drop of the FR dilute phase (P5-P13) with that of the SR dilute phase (P25-P30), it was found that the former was lower than the latter, so the entrainment capacity of the FR was lower than that of the SR.

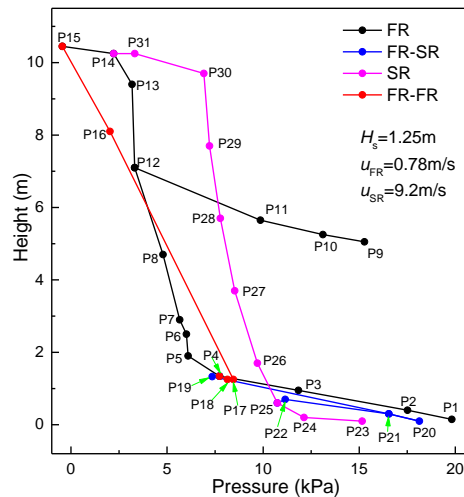


Figure 3. Pressure profile of the 1.5 MW_{th} CLC cold flow model ($d_{50}=122 \mu m$)

3.2 Effect of operational variables on solid circulation rate

In this section, the effects of five vital variables, including the FR gas velocity (u_{FR}), LS gas velocity (u_{LS}), SR gas velocity (u_{SR}), static bed height (H_s) and particle size, on the solid circulation rate (G_s) are investigated.

The effect of the u_{FR} and H_s on the G_s is shown in Figure 4(a). When the u_{FR} was in the range of 0.1 ~ 0.78 m/s, the change trend of the G_s under different H_s was different. For the $H_s = 0.75$ m, the top of the bed level was lower than the overflow port. With the increase in the u_{FR} , more bubbles were generated, and the amount of solid particles elutriated into the freeboard increased, resulting in an increase in the G_s from 12.72 kg/(m²·s) to 36.85 kg/(m²·s). For the $H_s = 1.05$ m, the top of bed level was at the overflow port but not full. The solid particles elutriated into the freeboard increased with increasing u_{FR} , and the solid fraction in the overflow port decreased, so the G_s decreased from 79.45 kg/(m²·s) to 67.93 kg/(m²·s). For the $H_s = 1.25$ m and $H_s = 1.45$ m, the tops of the bed level were higher than those of the overflow port. The frequency of bubble coalescence and breakage in the dense phase increased with the increasing u_{FR} , and the particle motion passing through the overflow port was enhanced, so the G_s increased. The G_s decreased with increasing u_{FR} from 0.78 m/s to 1.01 m/s. This is because the u_{FR} of 0.78 m/s is the transition velocity (U_c) for small particles ($d_{50} = 122$ μm), i.e., when the $u_{FR} > 0.78$ m/s, the fluidization regime of the TFB changes from the bubbling regime to the turbulent regime, and the fluidization characteristics change accordingly. In the turbulent regime, the entrainment capacity is strengthened, more particles are carried into the annular CS and the height of the TFB dense phase is decreased, so the amount of solid particles passing through the overflow port is reduced.

When the u_{FR} was constant, the G_s increased significantly with increasing H_s from 0.75 m to 1.25 m, while the H_s increased from 1.25 m to 1.45 m resulting in only

a slight increase in the G_s . As the H_s increased from 0.75 m to 1.45 m, the average value of error bars increased from 2.92 kg/(m²·s) to 11.1 kg/(m²·s), and this indicated that the material fluctuation of the cold flow model increased with the increasing H_s . Under different u_{FR} , the differences in the G_s of $H_s = 1.25$ m and $H_s = 1.45$ m were different, and the average difference was calculated to be 13.9 kg/(m²·s), which was slightly larger than the average value of error bars (11.1 kg/(m²·s)). The results indicated that when the H_s was lower than the overflow port (1.25 m), the G_s increased rapidly with increasing H_s , while when the H_s was higher than the overflow port, the G_s increased slightly with increasing H_s . Therefore, to prevent the overflow port from becoming a constraint factor on the G_s , the H_s should be higher than the overflow port. Figure 4(b) shows the change in the pressure drop of the SR dilute phase (P29-P30) with the u_{FR} and H_s . Comparing Figure 4(a) with Figure 4(b), it was found that the changes of the G_s and the pressure drop of P29-P30 were similar.

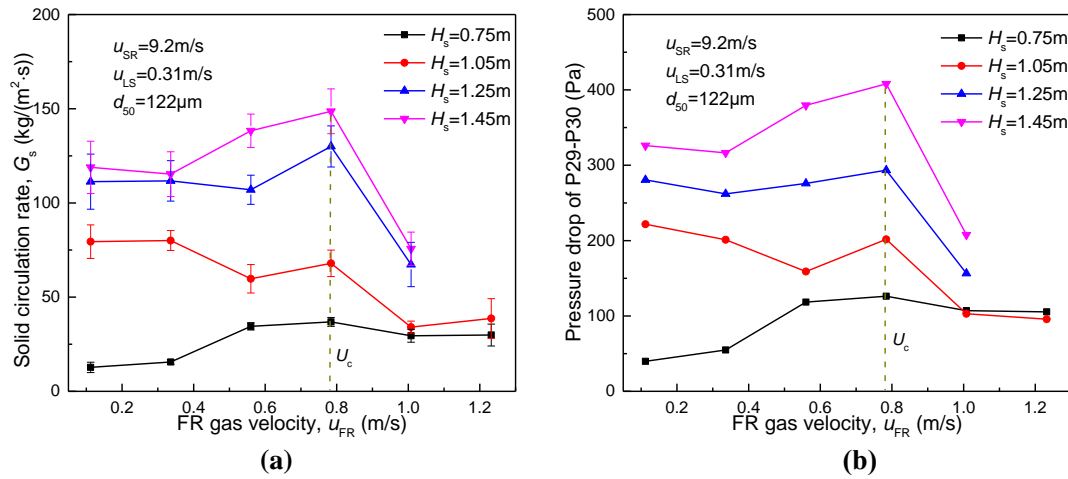


Figure 4. Effect of the u_{FR} and H_s on (a) solid circulation rate and (b) pressure drop of P29-P30

The effect of the particle size and u_{FR} on the G_s is depicted in Figure 5(a). With the increase in the particle size, the change trend of the G_s was different in different u_{FR} ranges. When the u_{FR} was in the range of 0.1 ~ 0.78 m/s, the G_s of small particles ($d_{50} = 122$ μ m) was the highest among the three different solid particles, but when the $u_{FR} >$

0.78 m/s, the G_s of small particles ($d_{50} = 122 \mu\text{m}$) decreased rapidly from 129.98 $\text{kg}/(\text{m}^2\cdot\text{s})$ to 67.32 $\text{kg}/(\text{m}^2\cdot\text{s})$ and became the lowest. For three different particle sizes, the variation trend was similar with increasing u_{FR} . The transition velocity is different for different particle sizes (as shown in Table 1), so the u_{FR} corresponding to the decrease in the G_s is different, as shown in Figure 5(a). Lyngfelt and Leckner³⁵ pointed out that the G_s of CLC unit was 25.5 $\text{kg}/(\text{m}^2\cdot\text{s})$ in the 1000 MW_{th} solid-fuel CLC design. The maximum G_s could approach 130 $\text{kg}/(\text{m}^2\cdot\text{s})$ in this work, which indicated that the G_s value satisfied the requirements of CLC auto-thermal operation. With the increase in the particle size from 122 μm to 392 μm , the average value of error bars decreased slightly from 11.05 $\text{kg}/(\text{m}^2\cdot\text{s})$ to 8.47 $\text{kg}/(\text{m}^2\cdot\text{s})$, which indicated that increasing particle size could alleviate the material fluctuation of the cold flow model. A good gas-solid contact will facilitate chemical reactions, and the gas-solid contact in the bubbling regime is inferior to that in the turbulent regime. Therefore, to maintain a good gas-solid contact and high G_s , the transition velocity is adopted as the operational velocity of the FR. Figure 5(b) shows the effect of the u_{FR} and particle size on the pressure drop of the SR dilute phase. Comparing Figure 5(a) with Figure 5(b), a correlation between the pressure drop of the SR dilute phase and the G_s should exist, since the latter has a similar trend to the former.

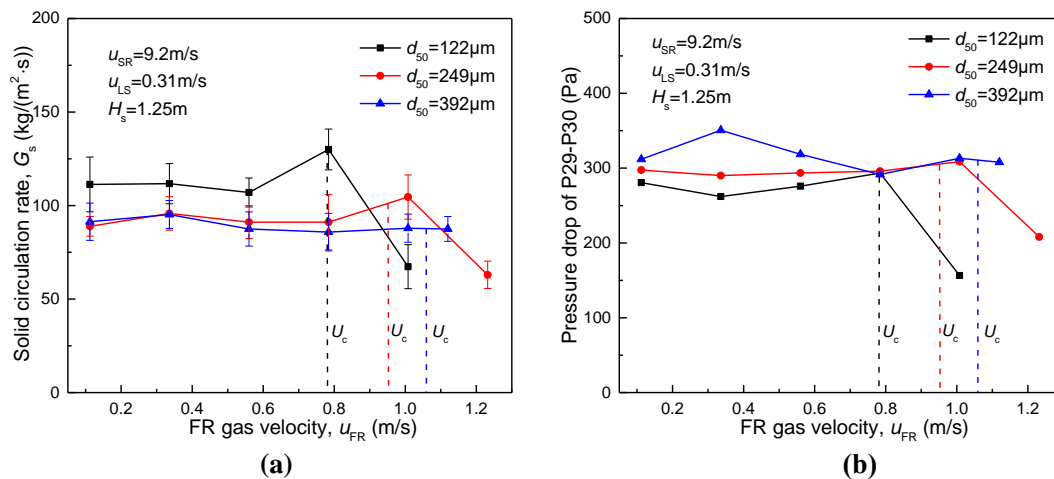


Figure 5. Effect of the u_{FR} and particle size on (a) solid circulation rate and (b) pressure drop

of P29-P30

Figure 6(a) shows the effect of the u_{LS} and H_s on the G_s . With the increase in the u_{LS} , the change trend of the G_s under different H_s was different. For the $H_s = 0.75$ m, the G_s remained almost unchanged ($27.95 \text{ kg}/(\text{m}^2 \cdot \text{s})$) with increasing u_{LS} ; for the $H_s = 1.05$ m, the G_s increased from $36.47 \text{ kg}/(\text{m}^2 \cdot \text{s})$ to $52.06 \text{ kg}/(\text{m}^2 \cdot \text{s})$ and then decreased to $45.67 \text{ kg}/(\text{m}^2 \cdot \text{s})$ with increasing u_{LS} ; and for the $H_s = 1.25$ m, the G_s first increased from $54.13 \text{ kg}/(\text{m}^2 \cdot \text{s})$ to $115.35 \text{ kg}/(\text{m}^2 \cdot \text{s})$ and then remained unchanged with increasing u_{LS} . The reason is as follows: when the H_s is lower than the overflow port, the G_s is mainly controlled by the H_s rather than the u_{LS} . When the H_s is higher than the overflow port, a large number of particles flow out through the overflow port, and the change in the u_{LS} will affect the G_s . The error bars at different H_s did not intersect, which indicated that the increase rate of the G_s with H_s was higher than the measurement error. In Figure 6(b), it can be seen that the change trend of the pressure drop of the SR dilute phase was the same as that of the G_s .

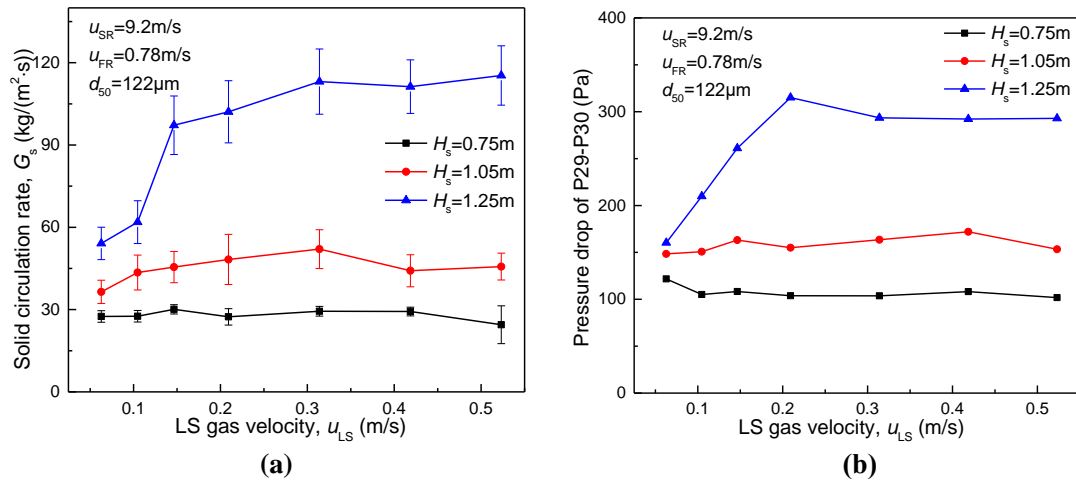


Figure 6. Effect of the u_{LS} and H_s on (a) solid circulation rate and (b) pressure drop of P29-

P30

Figure 7(a) shows the effect of the particle size and u_{LS} on the G_s . As the u_{LS} increased from 0.06 m/s to 0.52 m/s, the G_s with $d_{50} = 122, 249$ and $392 \mu\text{m}$ increased from $54.13 \text{ kg}/(\text{m}^2 \cdot \text{s})$ to $115.28 \text{ kg}/(\text{m}^2 \cdot \text{s})$, from $29.10 \text{ kg}/(\text{m}^2 \cdot \text{s})$ to $101.98 \text{ kg}/(\text{m}^2 \cdot \text{s})$

and from 0.00 kg/(m²·s) to 106.35 kg/(m²·s), respectively. This indicated that the u_{LS} could control the G_s . When the u_{LS} was in the range of 0.06 m/s to 0.31 m/s, the G_s decreased obviously with increasing particle size. This is because the minimum fluidization velocity for different particle sizes is different, the fluidization number corresponding to the same gas velocity is also different, and the smaller particles have a larger fluidization number and a stronger entrainment capacity. When the u_{LS} was in the range of 0.31 m/s to 0.52 m/s, the fluidization number was relatively large for different particle sizes, so the G_s decreased slightly with increasing particle size. With increase in the u_{LS} , the error bars of different particle sizes changed from disjoint to intersect, which also indicated that the G_s difference of different particle sizes decreased, as shown in Figure 7(a). Figure 7(b) shows the change in the pressure drop of the SR dilute phase with the u_{LS} and particle size. As mentioned above, the change trends of the pressure drop of the SR dilute phase and the G_s were basically similar.

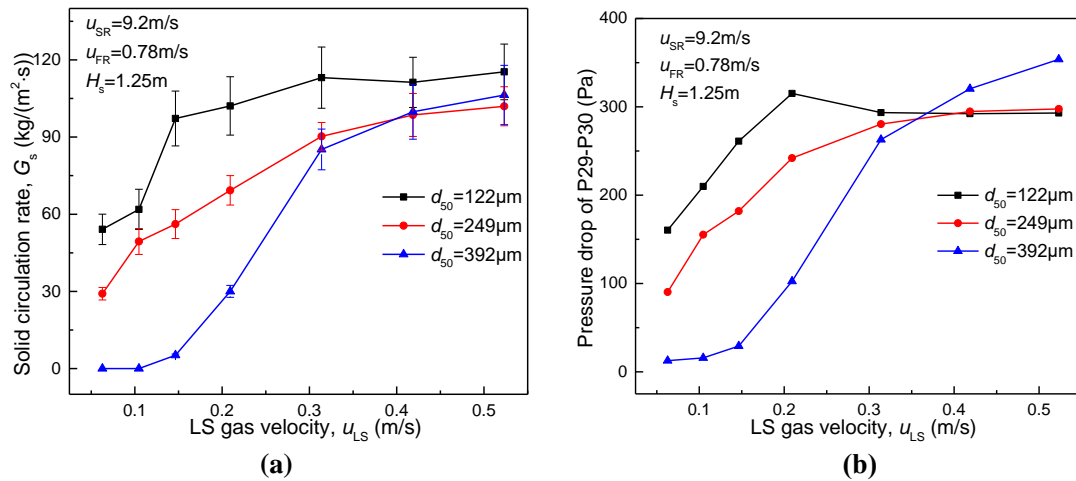


Figure 7. Effect of the u_{LS} and particle size on (a) solid circulation rate and (b) pressure drop of P29-P30

Figure 8(a) shows the effect of the u_{SR} and H_s on the G_s . As mentioned above, when the H_s was lower than the overflow port, the G_s was mainly controlled by the H_s . Therefore, when the $H_s = 0.75 \text{ m}$ or $H_s = 1.05 \text{ m}$, with the increase in the u_{SR} from 3.45 m/s to 11.50 m/s, the G_s first increased slightly and then remained unchanged, as shown

in Figure 8(a). When the $H_s = 1.25$ m, the G_s increased rapidly from 29.28 kg/(m²·s) to 122.16 kg/(m²·s) with increasing u_{SR} . This is because the H_s is higher than the overflow port and no longer controls the G_s . The effect of the u_{SR} and H_s on the pressure drop of the SR dilute phase is shown in Figure 8(b). Different from the above, the change trend of the pressure drop of the SR dilute phase with the u_{SR} or H_s was different from that of the G_s . This is because the fluidization regime of the SR changes from fast fluidized regime to transport regime with increasing u_{SR} , and different fluidization regimes have different fluidization characteristics.

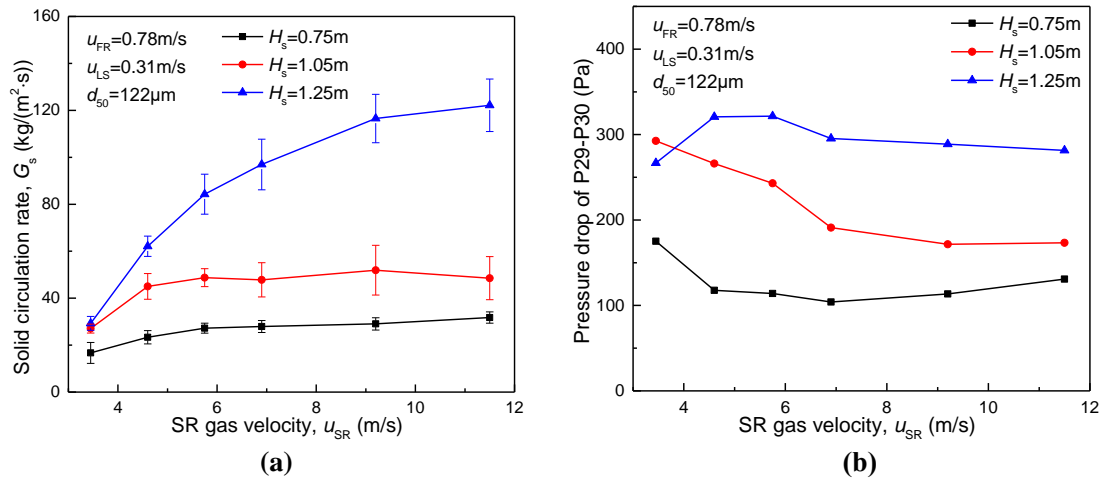


Figure 8. Effect of the u_{SR} and H_s on (a) solid circulation rate and (b) pressure drop of P29-

P30

Figure 9(a) shows the effect of the u_{SR} and particle size on the G_s . The G_s decreased with increasing particle size. For example, when the $u_{SR} = 9.2$ m/s, with the increase in the particle size from 122 μm to 392 μm, the G_s decreased from 116.52 kg/(m²·s) to 83.42 kg/(m²·s). This is because the terminal velocity of solid particles increases with increasing particle size, and smaller particles are more easily carried out of the reactor at a constant gas velocity. The average value of error bars decreased from 9.02 kg/(m²·s) to 4.22 kg/(m²·s) with increasing particle size, which indicated that the material fluctuation of the cold flow model was alleviated with increasing particle size. Figure 9(b) shows the effect of the u_{SR} and particle size on the pressure drop of the SR dilute

phase. With the increase in the u_{SR} or particle size, the change trend of the pressure drop of the SR dilute phase was inconsistent, but the variation range was very small.

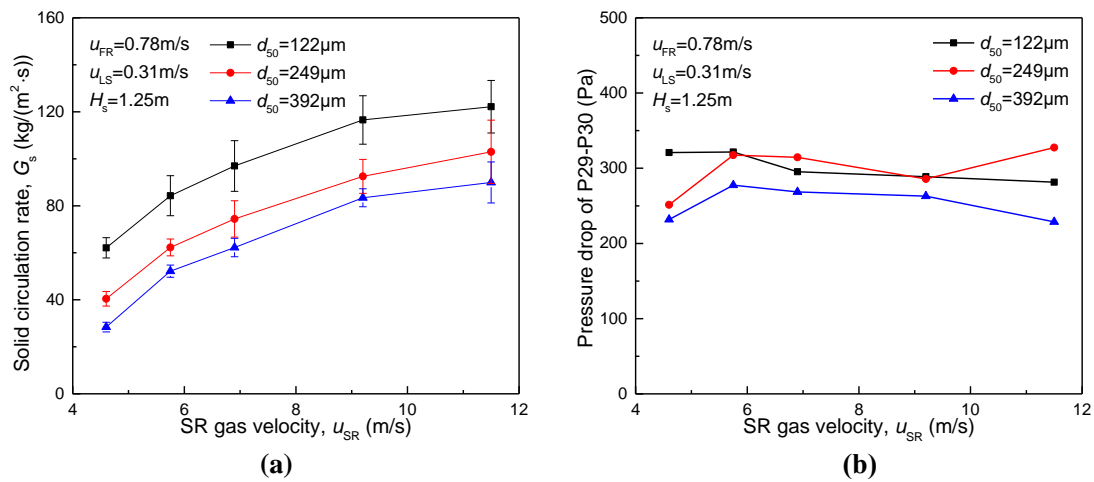


Figure 9. Effect of the u_{SR} and particle size on (a) solid circulation rate and (b) pressure drop of P29-P30

A correlation between the pressure drop of the SR dilute phase and the G_s is shown in Figure 10. The pressure drop of the SR dilute phase was linearly correlated with the G_s at the $u_{SR} = 9.2$ m/s. When measuring the G_s is inconvenient, the pressure drop of the SR dilute phase can be used to estimate the G_s . Quartz sands with different particle sizes have different physical properties and fluidization characteristics at the same gas velocity. Therefore, the correlations between the pressure drop of the SR dilute phase and the G_s with different particle sizes are different, as shown in equation (5). The negative intercept of equation (5) is caused by the pressure drop of the SR fluidizing gas. It should be noted that when the u_{SR} changes, the correlation will also change due to the change in the particle force and fluidization regime.

$$\begin{aligned}
 d_{50} = 122 \mu\text{m} : G_s &= 0.44 \Delta P_{29-30} - 17.74 \\
 d_{50} = 249 \mu\text{m} : G_s &= 0.32 \Delta P_{29-30} - 3.47 \\
 d_{50} = 392 \mu\text{m} : G_s &= 0.29 \Delta P_{29-30} - 1.16
 \end{aligned} \tag{5}$$

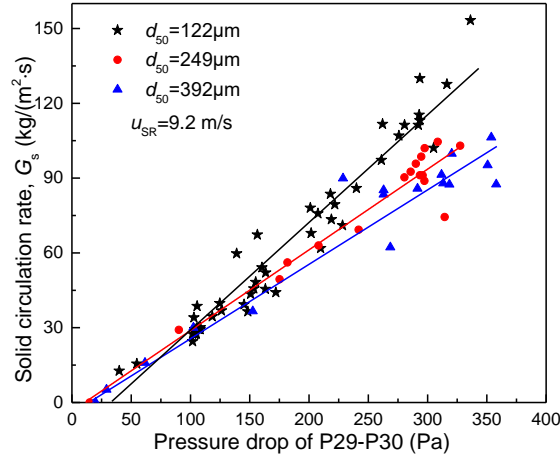


Figure 10. Correlation between the pressure drop of P29-P30 and the solid circulation rate

3.3 Effect of operational variables on hydrodynamic characteristics of simplified air reactor riser

The effect of different operational variables on the solid fraction profile of the SR is depicted in Figure 11. In Figure 11(a), when the u_{FR} increased from 0.11 m/s to 0.78 m/s, the solid fraction profile of the SR remained almost unchanged; while when the $u_{FR} > 0.78$ m/s, the solid fraction profile of the SR was deduced. The reason is below: the u_{FR} of 0.78 m/s is the transition velocity for small particles ($d_{50} = 122 \mu\text{m}$), i.e., when the $u_{FR} > 0.78$ m/s, the fluidization regime changes to the turbulent regime. In the turbulent regime, the entrainment capacity is strengthened, more quartz sand particles are carried into the annular CS and the amount of particles passing through the overflow port is reduced.

Figure 11(b) shows the effect of the u_{LS} on the solid fraction profile of the SR. With the increase in the u_{LS} , the solid fraction profile of the SR first increased quickly, then increased moderately and finally remained unchanged. When the $u_{LS} < 0.15$ m/s, the fluidization number is relatively small, and the solid flux from LS to SR is small and sensitive to the change in the u_{LS} . When the u_{LS} is between 0.15 m/s and 0.31 m/s, the solid flux from LS to SR increases slowly with increasing u_{LS} . When the $u_{LS} > 0.31$

m/s, the solid flux from LS to SR is insensitive to the change in the u_{LS} , and the limiting factor of the solid fraction profile of the SR changes from the u_{LS} to the u_{SR} or overflow characteristics.

Figure 11(c) shows the effect of the u_{SR} on the solid fraction profile of the SR. With the increase in the u_{SR} , the change trend of the solid fraction at different SR heights was different. In the range of SR heights from 0 m to 4 m, the solid fraction first decreased significantly and then became moderate with increasing u_{SR} . In the range of SR heights from 4 m to 10.45 m, the solid fraction was basically unchanged with increasing u_{SR} . There are two main reasons: 1) From the perspective of particle force, as the u_{SR} increases, the drag force on particles increases, and the distance required to accelerate from static state to slip velocity decreases, resulting in a decrease in the particle amount in the acceleration region. 2) From the perspective of the fluidization regime, the fluidization regime of the SR gradually transfers from the fast fluidized regime to the transport regime with increasing u_{SR} , and different fluidization regimes have different fluidization characteristics. For different fluidization regimes, the solid fraction of the dense phase or transition phase has a relatively large difference. In this work, when the SR height ranges from 0 m to 4 m, it is in the dense phase or transition phase and the solid fraction displays a large difference, as shown in Figure 11(c). The solid fraction of the dilute phase is generally one order of magnitude lower than that of the dense phase. Compared with the dense phase, the difference in the solid fraction of the dilute phase for different fluidization regimes is very small, so it is basically unchanged.

Figure 11(d) shows the effect of the H_s on the solid fraction profile of the SR. As mentioned above, when the H_s was lower than the overflow port (1.25 m), the G_s increased with increasing H_s ; while when the H_s was higher than the overflow port, the

G_s remained almost unchanged with increasing H_s . The solid fraction of the SR is positively correlated with the G_s when the u_{SR} remains unchanged. Therefore, the solid fraction profile of the SR increased with increasing H_s from 0.75 m to 1.25 m, while the solid fraction profile of the SR remained almost unchanged with increasing H_s from 1.25 m to 1.45 m.

Figure 11(e) shows the effect of the particle size on the solid fraction profile of the SR. With the increase in the particle size, the change trend of the solid fraction in the SR with different heights was inconsistent. When the SR height was less than 8 m, the solid fraction decreased with increasing particle size, while when the SR height was higher than 8 m, the solid particles accelerated to the slip velocity, so the solid fraction was unchanged with increasing particle size, as shown in Fig. 11(e).

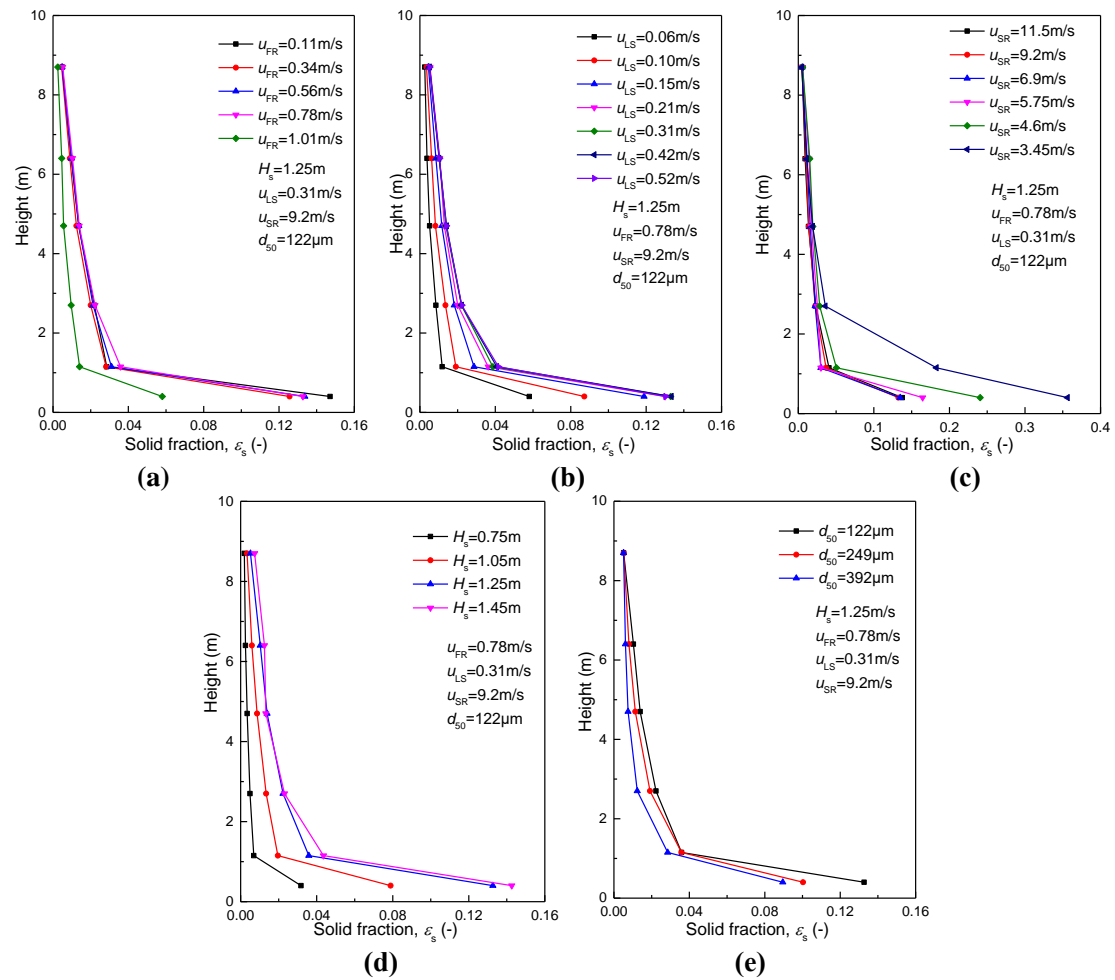


Figure 11. Solid fraction profiles of the SR at different static bed heights, gas velocities and

4. Discussion

Typical experimental results of the G_s and the pressure drop of the overflow port (P4-P19) are shown in Figure 12. The results show that the G_s is positively correlated with the pressure drop of the overflow port. Therefore, an overflow model is proposed to predict the G_s by using the pressure drop of the overflow port.

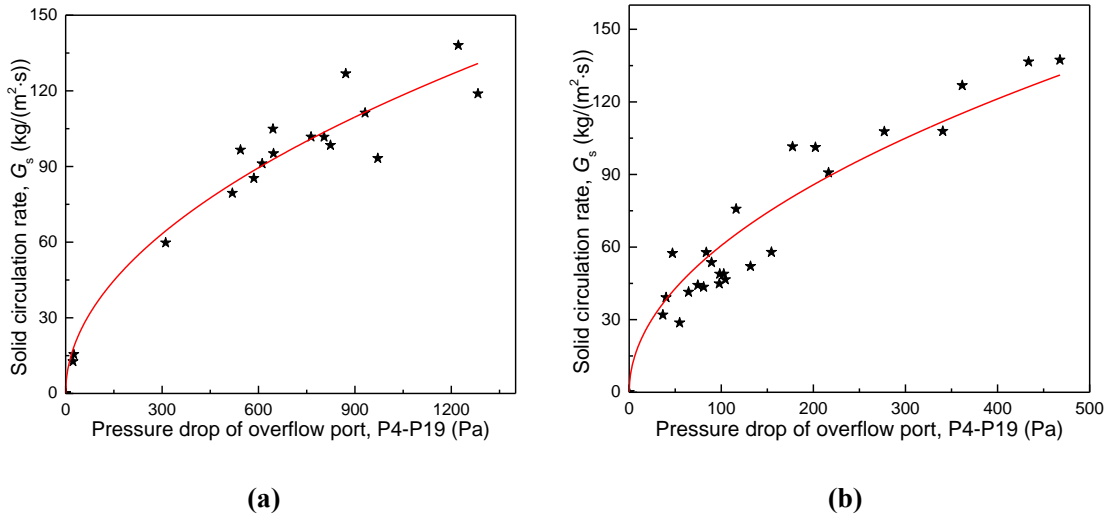


Figure 12. Correlation of the solid circulation rate and pressure drop of the overflow port (P4-P19): (a) FR in the bubbling regime and (b) FR in the turbulent regime

A schematic diagram of the fuel reactor and simplified riser is shown in Figure 13. The fluidized solid particles in the cold flow model are regarded as continuously flowing fluids, and a conservation equation can be obtained according to the theory of fluid mechanics:

$$P_4 + \rho_4 g H_4 + \rho_4 \frac{u_4^2}{2} = P_{19} + \rho_{19} g H_{19} + \rho_{19} \frac{u_{19}^2}{2} + h_f \quad (6)$$

where P_i represents the pressure of port i , Pa; ρ_i represents the fluid density of port i , kg/m³; H_i represents the height of port i , m; u_i represents the horizontal direction velocity of port i , m/s; and h_f represents the resistance loss from port 4 to port 19,

kg/(m·s²).

In Figure 13, it can be seen that H_4 and ρ_4 are equal to H_{19} and ρ_{19} , respectively.

It is assumed that the horizontal direction velocity of port 4 is 0 m/s, i.e., $u_4 = 0$ m/s;

therefore, equation (6) can be simplified to equation (7):

$$P_4 = P_{19} + \rho_{19} \frac{u_{19}^2}{2} + h_f \quad (7)$$

For ease of expression and calculation, h_f is set as $h_f = \lambda \rho_{19} \frac{u_{19}^2}{2}$, and equation (7) can be changed to:

$$P_4 = P_{19} + \rho_{19} \frac{u_{19}^2}{2} + \lambda \rho_{19} \frac{u_{19}^2}{2} \quad (8)$$

$$u_{19} = \sqrt{\frac{2(P_4 - P_{19})}{(1 + \lambda)\rho_{19}}} \quad (9)$$

The fluid density of port 19 (ρ_{19}) depends on the particle density and the solid fraction of the FR dense phase and is calculated by:

$$\rho_{19} = \rho_p \varepsilon_{sd} \quad (10)$$

where ε_{sd} represents the solid fraction of the FR dense phase, -.

Introducing equation (10) into equation (9), the solid velocity of the overflow port (u_{19}) can be expressed as:

$$u_{19} = \sqrt{\frac{2(P_4 - P_{19})}{(1 + \lambda)\rho_p \varepsilon_{sd}}} = c \sqrt{\frac{2(P_4 - P_{19})}{\rho_p \varepsilon_{sd}}} \quad (11)$$

$$c = \sqrt{\frac{1}{1 + \lambda}} \quad (c < 1) \quad (12)$$

The overflow pipe is inclined downward, and the connection between the overflow pipe and FR is an ellipse. The sectional area of the overflow port (S_{ov}) can be expressed as:

$$S_{ov} = \frac{\pi d_{ov}}{4} \frac{d_{ov}}{\cos(\pi/2 - \theta)} = \frac{\pi d_{ov}^2}{4 \sin \theta} \quad (13)$$

where d_{ov} represents the inner diameter of the overflow pipe, m; θ represents the angle between the overflow pipe and the vertical direction, -.

The overflow port may not be fully filled with solid particles. The ratio of the sectional area filled with solid particles to the sectional area of the overflow port is specified as e . The solid volume flux of the overflow port (\dot{Q}_{ov}) is estimated by:

$$\dot{Q}_{ov} = eS_{ov}u_{19} = e \frac{\pi d_{ov}^2}{4 \sin \theta} c \sqrt{\frac{2(P_4 - P_{19})}{\rho_p \varepsilon_{sd}}} = \beta \frac{\pi d_{ov}^2}{4 \sin \theta} \sqrt{\frac{2(P_4 - P_{19})}{\rho_p \varepsilon_{sd}}} \quad (\beta = ec) \quad (14)$$

The solid mass flux of the overflow port (\dot{m}_{ov}) is related to the fluid density and the solid volume flux of the overflow port, and it can be expressed as:

$$\dot{m}_{ov} = \rho_{19} \dot{Q}_{ov} = \rho_p \varepsilon_{sd} \beta \frac{\pi d_{ov}^2}{4 \sin \theta} \sqrt{\frac{2(P_4 - P_{19})}{\rho_p \varepsilon_{sd}}} = \beta \frac{\pi d_{ov}^2}{4 \sin \theta} \sqrt{2(P_4 - P_{19}) \rho_p \varepsilon_{sd}} \quad (15)$$

Based on the mass balance, the solid mass flux of the overflow port (\dot{m}_{ov}) is equal to the solid mass flux of the SR (\dot{m}_{SR}). Combined with the sectional area of the SR, the G_s is expressed by equation (16):

$$G_s = \frac{\dot{m}_{SR}}{S_{SR}} = \frac{\dot{m}_{ov}}{S_{SR}} = \beta \frac{\pi d_{ov}^2}{S_{SR} 4 \sin \theta} \sqrt{2(P_4 - P_{19}) \rho_p \varepsilon_{sd}} = \beta \frac{d_{ov}^2}{d_{SR}^2 \sin \theta} \sqrt{2(P_4 - P_{19}) \rho_p \varepsilon_{sd}} \quad (16)$$

where d_{SR} represents the inner diameter of the simplified riser, m.

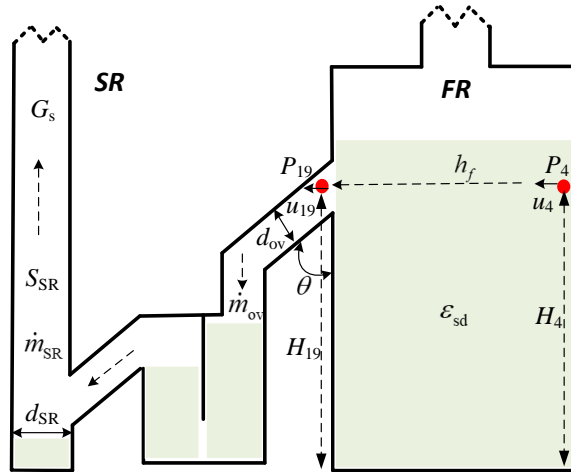


Figure 13. Schematic diagram of the fuel reactor and simplified riser

In equation (16), d_{ov} , d_{SR} and θ are the design parameters, ρ_p is the physical parameter of particles, P_4-P_{19} can be measured in the cold flow model, and ε_{sd} is calculated by the pressure drop of the FR dense phase. Therefore, the value of constant β can be obtained by using the experimental results of the cold flow model. Through calculation, the values of β in the bubbling regime and turbulent regime were different, and the results were 0.0537 and 0.102, respectively, as shown in equations (17) and (18). The value of β in the bubbling regime is smaller than that in the turbulent regime, which may be because the solid particles in the turbulent regime operate more violently and flow out more easily from the overflow port.

$$\text{Bubbling regime: } G_s = 0.0537 \frac{d_{ov}^2}{d_{SR}^2 \sin \theta} \sqrt{2(P_4 - P_{19}) \rho_s \varepsilon_{sd}} \quad (17)$$

$$\text{Turbulent regime: } G_s = 0.102 \frac{d_{ov}^2}{d_{SR}^2 \sin \theta} \sqrt{2(P_4 - P_{19}) \rho_s \varepsilon_{sd}} \quad (18)$$

The results of the G_s calculated by equations (17) and (18) were compared with the experimental data, and the results are shown in Figure 14. The relative errors were mostly within 25%, which indicated that the fitted value of β was reasonable. When measuring the G_s is inconvenient, equations (17) and (18) can be used to estimate it. In the CLC design process, equations (17) and (18) obtained in this work can be applied to determine whether the overflow port will become a limiting factor of the G_s or not. If the G_s of the overflow port is higher than the design value, this indicates that the overflow port is no longer the limiting factor of the G_s . Otherwise, the design of the overflow port is unreasonable and needs to be redesigned.

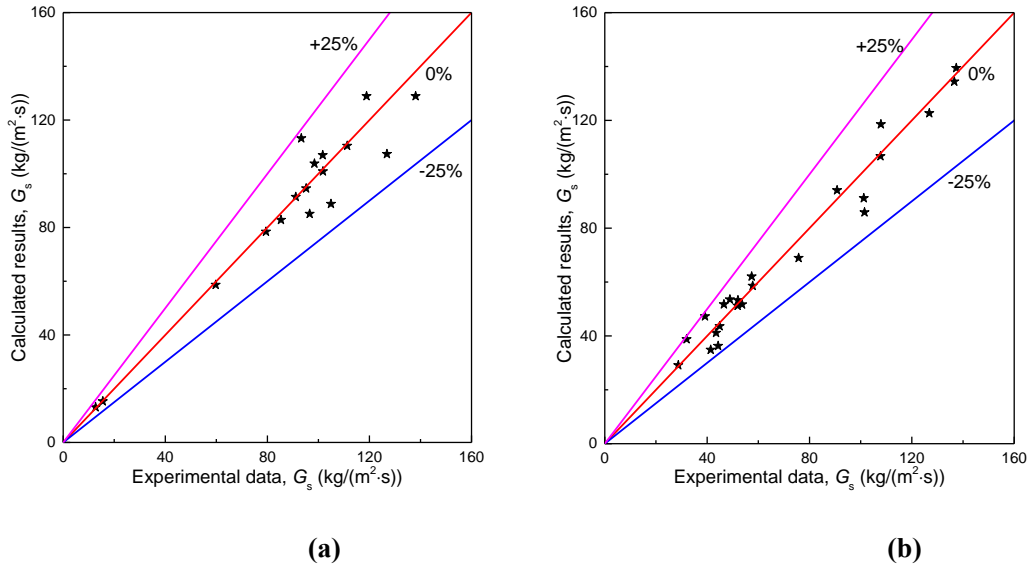


Figure 14. Comparison of the typical experimental data and the calculated results: (a) FR in the bubbling regime and (b) FR in the turbulent regime

5. Conclusion

A 1.5 MW_{th} CLC cold flow model consisting of a fuel reactor and a simplified air reactor riser was proposed and constructed to study the solid circulation characteristics. The solid circulation was controlled by the overflow method, and an overflow port was installed in the turbulent fluidized bed. Three kinds of quartz sands were selected as fluidized particles. Reasonable pressure profile was obtained in the 1.5 MW_{th} CLC cold flow model. The effects of different static bed heights, gas velocities and particle sizes on the solid circulation rate and hydrodynamic characteristics were discussed. The results showed that the maximum solid circulation rate approached 130 kg/(m²·s) and this value is sufficient to satisfy the requirements of CLC auto-thermal operation. The static bed height should be higher than the overflow port to prevent the overflow port from becoming a constraint condition. The transition velocity was adopted as the operational velocity of the fuel reactor to obtain a high solid circulation rate. An overflow model was developed to predict the solid circulation rate. The relative errors between the calculated results and the experimental data were within 25%, which

indicated that the overflow model could predict the solid circulation rate accurately. In the CLC design process, this overflow model could be applied to determine whether the overflow port will become a limiting factor of the solid circulation rate.

Acknowledgements

This research is funded from National Key Research and Development Plan of China (No 2017YFE0112500), and European Union's Horizon 2020 Research and Innovation Program (No 764697).

Nomenclature

AR	Air reactor
CLC	Chemical looping combustion
CS	Carbon stripper
d_{50}	Median particle diameter, μm
d_{ov}	Inner diameter of overflow pipe, m
d_{SR}	Inner diameter of simplified riser, m
e	Ratio of the sectional area filled with the particles to the sectional area of overflow port, -
FR	Fuel reactor
g	Gravity acceleration, m/s^2
G_s	Solid circulation rate, $\text{kg}/(\text{m}^2 \cdot \text{s})$
$G_{s,FR}$	Solid circulation rate of fuel reactor, $\text{kg}/(\text{m}^2 \cdot \text{s})$
$G_{s,t}$	Total solid circulation rate, $\text{kg}/(\text{m}^2 \cdot \text{s})$
h_f	Resistance loss, $\text{kg}/(\text{m} \cdot \text{s}^2)$
$H_{dip,i}$	Accumulative height of solid particle in the dipleg, m
H_i	Height of port i , m
H_s	Static bed height, m

LS	Loop seal
\dot{m}_{ov}	Solid mass flux of overflow port, kg/s
\dot{m}_{SR}	Solid mass flux of simplified riser, kg/s
OC	Oxygen carrier
P_i	Pressure of port i , Pa
$\Delta P/\Delta H$	Pressure gradient, Pa/m
PSD	Particle size distribution
\dot{Q}_{ov}	Solid volume flux of overflow port, m ³ /s
S_{dip}	Sectional area of dipleg, m ²
S_{ov}	Sectional area of overflow port, m ²
S_{SR}	Sectional area of simplified riser, m ²
SR	Simplified riser
$t_{dip,i}$	Elapsed of solid particles in the dipleg, s
TFB	Turbulent fluidized bed
u_{FR}	Gas velocity of fuel reactor, m/s
u_i	Horizontal direction velocity of port i , m/s
u_{LS}	Gas velocity of loop seal, m/s
u_{SR}	Gas velocity of simplified riser, m/s
U_c	Transition velocity, m/s
β	Fitting constant, -
ε_s	Solid fraction, -
ε_{sd}	Solid fraction of dense phase, -
θ	Angle between overflow pipe and vertical direction, -
ρ_b	Bulk density, kg/m ³
ρ_g	Gas density, kg/m ³
ρ_i	Fluid density of port i , kg/m ³
ρ_p	Particle density, kg/m ³

References

1. Abanades, J. C.; Arias, B.; Lyngfelt, A.; Mattisson, T.; Wiley, D. E.; Li, H.; Ho, M. T.; Mangano, E.; Brandani, S. Emerging CO₂ capture systems. *Int. J. Greenhouse Gas Control* **2015**, *40*, 126-166.
2. Global Energy & CO₂ Status Report: The latest trends in energy and emissions in 2017.
3. Kanniche, M.; Gros-Bonnivard, R.; Jaud, P.; Valle-Marcos, J.; Amann, J.-M.; Bouallou, C. Pre-combustion, post-combustion and oxy-combustion in thermal power plant for CO₂ capture. *Appl. Therm. Eng.* **2010**, *30*, (1), 53-62.
4. Boot-Handford, M. E.; Abanades, J. C.; Anthony, E. J.; Blunt, M. J.; Brandani, S.; Mac Dowell, N.; Fernandez, J. R.; Ferrari, M. C.; Gross, R.; Hallett, J. P.; Haszeldine, R. S.; Heptonstall, P.; Lyngfelt, A.; Makuch, Z.; Mangano, E.; Porter, R. T. J.; Pourkashanian, M.; Rochelle, G. T.; Shah, N.; Yao, J. G.; Fennell, P. S. Carbon capture and storage update. *Energy Environ. Sci.* **2014**, *7*, (1), 130-189.
5. Adanez, J.; Abad, A.; Mendiara, T.; Gayan, P.; de Diego, L. F.; Garcia-Labiano, F. Chemical looping combustion of solid fuels. *Prog. Energy Combust. Sci.* **2018**, *65*, 6-66.
6. Richter, H. J.; Knoche, K. F. Reversibility of combustion processes. *ACS Symp. Ser.* **1983**, *235*, 71-85.
7. Lyngfelt, A.; Leckner, B.; Mattisson, T. A fluidized-bed combustion process with inherent CO₂ separation; application of chemical-looping combustion. *Chem. Eng. Sci.* **2001**, *56*, (10), 3101-3113.
8. Berguerand, N.; Lyngfelt, A. Design and operation of a 10 kW_{th} chemical-looping combustor for solid fuels - Testing with South African coal. *Fuel* **2008**, *87*, (12), 2713-2726.
9. Stroehle, J.; Orth, M.; Epple, B. Design and operation of a 1 MW_{th} chemical looping plant. *Appl. Energy* **2014**, *113*, 1490-1495.
10. Cheng, M. Experimental investigation on coal-fired chemical looping combustion coupled with an annular carbon stripper. Tsinghua University, Beijing, China, 2018.
11. Kim, H. R.; Wang, D.; Zeng, L.; Bayham, S.; Tong, A.; Chung, E.; Kathe, M. V.; Luo, S.; McGiveron, O.; Wang, A.; Sun, Z.; Chen, D.; Fan, L.-S. Coal direct chemical looping combustion process: Design and operation of a 25 kW_{th} sub-pilot unit. *Fuel* **2013**, *108*, 370-384.
12. Wang, X.; Jin, B.; Zhu, X.; Liu, H. Experimental evaluation of a novel 20 kW_{th} in situ gasification chemical looping combustion unit with an iron ore as the oxygen carrier. *Ind. Eng. Chem. Res.* **2016**, *55*, (45), 11775-11784.
13. Markstrom, P.; Linderholm, C.; Lyngfelt, A., Chemical-looping combustion of solid fuels - Design and operation of a 100 kW unit with bituminous coal. *Int. J. Greenhouse Gas Control* **2013**, *15*, 150-162.
14. Abad, A.; Perez-Vega, R.; de Diego, L. F.; Garcia-Labiano, F.; Gayan, P.; Adanez, J. Design and operation of a 50 kW_{th} chemical looping combustion (CLC) unit for solid fuels. *Appl. Energy* **2015**, *157*, 295-303.
15. Shen, L.; Wu, J.; Gao, Z.; Xiao, J. Reactivity deterioration of NiO/Al₂O₃ oxygen carrier for chemical looping combustion of coal in a 10 kW_{th} reactor. *Combust. Flame* **2009**, *156*, (7), 1377-1385.
16. Sozinho, T.; Pelletant, W.; Yazdanpanah, M.; Bertholin, S. Petcoke chemical looping combustion in a continuous 10 kW_{th} pilot plant. *Abstr. Pap. Am. Chem. Soc.* **2013**, 245.
17. Ma, J.; Tian, X.; Wang, C.; Chen, X.; Zhao, H. Performance of a 50 kW_{th} coal-fuelled chemical looping combustor. *Int. J. Greenhouse Gas Control* **2018**, *75*, 98-106.
18. Chen, H.; Cheng, M.; Liu, L.; Li, Y.; Li, Z.; Cai, N. Coal-fired chemical looping combustion coupled with a high-efficiency annular carbon stripper. *Int. J. Greenhouse Gas Control* **2020**, *93*, 102889.
19. Lighty, J.; Whitty, K.; Smith, P.; Eyring, T. Chemical looping with oxygen uncoupling with coal. *NETL CO₂ capture technology meeting*, 2012.
20. Ohlemueller, P.; Busch, J.-P.; Reitz, M.; Stroehle, J.; Epple, B., Chemical-looping combustion of hard coal: autothermal operation of a 1 MW_{th} pilot plant. *J. Energy Resour. Technol.-Trans. ASME* **2016**, *138*, (4), 042203.
21. Abdulally, I.; Andrus, H. E.; Edberg, C.; Chiu, J.; Thibeault, P.; Lani, B. ALSTOM's chemical looping combustion prototype for CO₂ capture from existing pulverized coal fired power plants. *NETL CO₂ capture technology meeting*, 2012.
22. Markstrom, P.; Linderholm, C.; Lyngfelt, A. Operation of a 100 kW chemical-looping combustor with Mexican petroleum coke and Cerrejon coal. *Appl. Energy* **2014**, *113*, 1830-1835.
23. Stroehle, J.; Orth, M.; Epple, B. Chemical looping combustion of hard coal in a 1 MW_{th} pilot plant using ilmenite as oxygen carrier. *Appl. Energy* **2015**, *157*, 288-294.
24. Proell, T.; Kolbitsch, P.; Bolhar-Nordenkamp, J.; Hofbauer, H. A novel dual circulating fluidized bed system for chemical looping processes. *AIChE J.* **2009**, *55*, (12), 3255-3266.
25. Stollhof, M.; Penthor, S.; Mayer, K.; Hofbauer, H. Fluid dynamic evaluation of a 10 MW scale reactor design for chemical looping combustion of gaseous fuels. *Chem. Eng. Sci.* **2018**, *178*, 48-60.

26. Dubey, A. K.; Samanta, A.; Sarkar, P.; Karmakar, M. K.; Mukherjee, A.; Loha, C.; Kumar, M.; Sahu, S. G.; Saxena, V. K.; Chatterjee, P. K. Hydrodynamic characteristics in a pilot-scale cold flow model for chemical looping combustion. *Adv. Powder Technol.* **2018**, 29, (6), 1499-1506.
27. Bischi, A.; Langorgen, O.; Morin, J.-X.; Bakken, J.; Ghorbaniyan, M.; Bysveen, M.; Bolland, O. Hydrodynamic viability of chemical looping processes by means of cold flow model investigation. *Appl. Energy* **2012**, 97, 201-216.
28. Liu, Y.; Chen, S.; Zhu, M.; Soomro, A.; Xiang, W. Investigation of a dual cold-flow fluidized bed for calcium looping gasification process. *Powder Technol.* **2019**, 353, 10-19.
29. Alghamdi, Y.; Peng, Z.; Zanganeh, J.; Moghtaderi, B.; Doroodchi, E. Hydrodynamics similarities in cold flow model of chemical looping combustors: An experimental study. *Powder Technol.* **2019**, 343, 542-550.
30. Thon, A.; Kramp, M.; Hartge, E.-U.; Heinrich, S.; Werther, J. Operational experience with a system of coupled fluidized beds for chemical looping combustion of solid fuels using ilmenite as oxygen carrier. *Appl. Energy* **2014**, 118, 309-317.
31. Mayer, F.; Bidwe, A. R.; Schopf, A.; Taheri, A. K.; Zieba, M.; Scheffknecht, G. Comparison of a new micaceous iron oxide and ilmenite with respect to syngas conversion in a BFB reactor and adaptation of a 10 kW_{th} DFB system for CLC to solid fuels. *2nd International conference on chemical looping*, Darmstadt, Germany, 2012.
32. Chen, H.; Li, Z.; Liu, X.; Li, W.; Cai, N.; Tebianian, S.; Bertholin, S.; Yazdanpanah, M.; Zhang, A. Cold model study of a 1.5 MW_{th} circulating turbulent fluidized bed fuel reactor in chemical looping combustion. *Energy Fuels* **2020**, 34, (7), 8575-8586.
33. Wen, C. Y.; Yu, Y. H., A generalized method for predicting minimum fluidization velocity. *AIChE J.* **1966**, 12, (3), 610-612.
34. Bi, H. T.; Grace, J. R.; Zhu, J. Regime transitions affecting gas-solids suspensions and fluidized-beds. *Chem. Eng. Res. Des.* **1995**, 73, (A2), 154-161.
35. Lyngfelt, A.; Leckner, B. A 1000 MW_{th} boiler for chemical-looping combustion of solid fuels - Discussion of design and costs. *Appl. Energy* **2015**, 157, 475-487.

Abstract Graphics

